ROYAL SOCIETY
OF CHEMISTRY

PAPER

CrossMark
click for updates

Alumina-supported sub-nanometer Pt_{10} clusters: amorphization and role of the support material in a highly active CO oxidation catalyst†

Chunrong Yin,‡[a] Fabio R. Negreiros,‡[b] Giovanni Barcaro,‡[b] Atsushi Beniya,‡[c] Luca Sementa,[b] Eric C. Tyo,[a] Stephan Bartling,[d] Karl-Heinz Meiwes-Broer,[d] Sönke Seifert,[e] Hirohito Hirata,[f] Noritake Isomura,[c] Sandeep Nigam,[g] Chiranjib Majumder,[g] Yoshihide Watanabe,*[c] Alessandro Fortunelli*[bh] and Stefan Vajda*[a]

Catalytic CO oxidation is unveiled on size-selected Pt_{10} clusters deposited on two very different ultrathin ($\approx 0.5-0.7$ nm thick) alumina films: (i) a highly ordered alumina obtained under ultra-high vacuum (UHV) by oxidation of the NiAl(110) surface and (ii) amorphous alumina obtained by atomic layer deposition (ALD) on a silicon chip that is a close model of real-world supports. Notably, when exposed to realistic reaction conditions, the Pt_{10}/UHV-alumina system undergoes a morphological transition in both the clusters and the substrate, and becomes closely akin to Pt_{10}/ALD-alumina, thus reconciling UHV-type surface-science and real-world experiments. The Pt_{10} clusters, thoroughly characterized via combined experimental techniques and theoretical analysis, exhibit among the highest CO oxidation activity per Pt atom reported for CO oxidation catalysts, due to the interplay of ultra-small size and support effects. A coherent interdisciplinary picture then emerges for this catalytic system.

[a]*Materials Science Division and Nanoscience & Technology Division, Argonne National Laboratory, Lemont, Illinois, USA. E-mail: vajda@anl.gov*

[b]*CNR-ICCOM & IPCF, Consiglio Nazionale delle Ricerche, Pisa, Italy. E-mail: alessandro.fortunelli@cnr.it*

[c]*Frontier Research Center, Toyota Central R&D Labs. Inc., Nagakute, Aichi, Japan. E-mail: e0827@mosk.tytlabs.co.jp*

[d]*Institut für Physik, Universität Rostock, Rostock, Germany*

[e]*X-ray Science Division, Argonne National Laboratory, Lemont, Illinois, USA*

[f]*Advanced Material Engineering Div., Toyota Motor Corporation, Susono, Shizuoka, Japan*

[g]*Chemistry Division, Bhabha Atomic Research Centre, Trombay, Mumbai-400 085, India*

[h]*Materials and Process Simulation Center, California Institute of Technology, Pasadena, California, USA*

† Electronic supplementary information (ESI) available: Methods, Arrhenius plot; *in situ* XANES spectra of Pt_{10} clusters on ALD alumina; topographic STM images of the Pt_{10}/Al_2O_3/NiAl(110) system and histograms of the apparent cluster height and histograms of the apparent cluster aspect ratio; STM line profiles (as-prepared system and after exposure to CO and O_2); STM images of the Pt_{10}/Al_2O_3/NiAl(110) system (as-prepared, after exposure to gases and function of temperature); LEED images of Al_2O_3/NiAl(110) and Pt_{10}/Al_2O_3/NiAl(110); XPS spectra of Pt_{10} clusters on Al_2O_3/NiAl(110) after CO and O_2 gas exposure; calculated structures of free and supported Pt_{10} clusters and with adsorbed O_2 molecules and O atoms and with coadsorbed CO; calculated energy plot as a function of time on gas phase Pt_{10} clusters; Bader charge analysis on select configurations. See DOI: 10.1039/c6ta10989f

‡ C. Y., F. R. N., G. B., and A. B. contributed equally to this work.

1. Introduction

The catalytic oxidation of carbon monoxide to CO_2 on platinum catalysts has been extensively studied[1] due to its importance for fundamental understanding and its technological relevance in automotive catalytic converters[2] and fuel cells.[3] Vast efforts have been devoted to Pt single crystals or crystalline nanoparticles.[4,5] Recently, subnanometer metal clusters have proven to be effective catalysts in CO oxidation, down to CO oxidation by single Pt-atoms,[6,7] although poisoning of the single Pt atoms by CO in contrast to larger particles has also been reported.[8]

The unique electronic structure of subnanometer (or ultra-nano) clusters can be tuned by selecting the cluster size with atomic precision and the catalytic propensities of these materials are often dramatically altered by removing or adding a single (ad)atom.[9-15] Since the major fraction of the atoms in a subnanometer cluster are exposed to reactants, this size regime allows for a very economic use of precious metals as well. Moreover, the performance of ultrasmall clusters can be further optimized *via* support effects, see ref. 16-18 as examples. Despite these intriguing properties, catalysis by well-defined subnanometer clusters still remains a largely unexplored field, especially under realistic conditions of pressure and temperature. The oxidation state of the active phase is another important aspect in heterogeneous catalysis,[19] but the oxidation state of Pt in catalytic CO oxidation remains contradictory, with metallic[20] or (mildly) oxidized[21] platinum proposed

This journal is © The Royal Society of Chemistry 2017

J. Mater. Chem. A, 2017, 5, 4923–4931 | 4923

as active species in CO oxidation. Thus, additional rigorous joint experimental and theoretical investigations that yield detailed information on well-defined systems are strongly needed. Fortunately, thanks to their smallness, exhaustive first-principles investigations are amenable on these systems, thus providing precise information which complements experimental characterization and allows for in-depth interpretation.[22] On the experimental side, deposition of single atoms and size-selected clusters represents an attractive possibility.[6,9,11,17,23–25] As far as the support is considered, to avoid charging during cluster deposition and characterization, ultrathin oxide films grown on conductive or semiconductive substrates, thin enough to be sufficiently conductive, represent an elegant solution[26] and have been extensively investigated under ultrahigh vacuum (UHV) conditions *via* surface-science techniques such as Scanning Tunneling Microscopy (STM) with atomic-scale resolution.[27,28] However, the huge difference between the reaction conditions and systems studied under UHV conditions and realistic pressures makes the relationship of the UHV studies with industrially relevant ones uncertain. Recent work then focused on amorphous ultrathin alumina films made by atomic layer deposition (ALD) on a naturally oxidized doped silicon chip.[23,24] These supports closely mimic those used in real-world applications, and can be used at realistic pressures without undergoing significant morphological modifications, but their relationships with the UHV-prepared ones are again unclear.

Here we take a step further with the goal of reconciling three approaches – experimental studies of subnanometer clusters under (i) UHV and (ii) realistic reaction conditions, accompanied by (iii) theoretical modeling – into one coherent picture. CO oxidation is first studied under realistic reaction conditions *in situ* on size-selected Pt_{10} clusters supported on an ultrathin amorphous ALD-alumina film. Grazing incidence X-ray absorption near edge spectroscopy (GIXANES) is used to monitor the evolution of the oxidation state of the clusters, and grazing incidence small angle X-ray scattering (GISAXS) to study the sintering resistance, while the activity of the clusters is monitored by temperature programmed reaction (TPRx) using on-line mass spectrometry.[19,23] In parallel, size-selected Pt_{10} clusters are deposited onto UHV-prepared crystalline alumina grown on the NiAl(110) single-crystal surface. STM is employed to characterize the shape of the as-prepared supported clusters, finding that they assume flat, two-dimensional configurations parallel to the alumina surface. This system is then subjected to identical working CO oxidation (COox) reaction conditions as applied to the Pt_{10}/ALD-alumina system. Low-energy electron diffraction (LEED) is used to monitor the restructuring of the oxide film, and morphological changes in the Pt_{10} clusters are revealed by STM, while X-ray photoelectron spectroscopy (XPS) provides information on the charge state of aluminum and carbon atoms. Finally, first-principles density functional theory (DFT) simulations are used to clarify the structure and COox catalytic mechanisms on Pt_{10}, both in the gas phase and deposited on a realistic structural model of an alumina surface. From the combination of these three approaches, a unified interdisciplinary view emerges. The Pt_{10} clusters on the ALD-grown alumina turn out to be robust (without any sign of sintering) and extremely active COox catalysts, actually exhibiting peak-performance per Pt atom reported so far, with an activation energy of ≈ 60 kJ mol^{-1} and a mild oxidation state in excellent agreement with theoretical predictions. Strikingly, when subjected to COox reaction conditions, the Pt_{10}/UHV-alumina/NiAl(110) model system is found to transform into an amorphous layer with three-dimensional Pt_{10} clusters which closely resembles the features of the Pt_{10}/ALD-alumina system, thus providing a missing link between surface-science and realistic systems.[29]

2. Results and discussion

Hereafter we present sequentially and discuss the results of the three approaches presented in the introduction: experimental studies of subnanometer clusters under (a) UHV and (b) realistic reaction conditions, and (c) theoretical modeling, at the same time underlying the links among them. In Section 3 we will then be able to draw the main conclusions of our analysis, while Section 4 provides a more detailed description of the methods here employed.

2.a *In situ* GISAXS/GIXANES/TPRx results on Pt_{10} clusters supported on ALD-alumina

The TPRx data for the CO_2 product during CO oxidation on Pt_{10}/Al_2O_3 are shown in Fig. 1a, along with the applied temperature ramp. The onset of CO_2 production is evident at 150 °C and the turn-over rate (TOR) reaches about 3350 CO_2 molecules produced by the Pt_{10} cluster per second (or 335 CO_2 molecules per Pt atom per second) at 300 °C. To the best of our knowledge, the highest COox activity was reported by Santra *et al.* for Pt(100), Rh(100) and Rh(110) single crystals[30] and by Yan *et al.* for oxide-supported Pt nanowires.[31,32] Yan *et al.* listed per surface site turn-over-frequency (TOF) in the order of 1500 molecules per site per s. Based on the plot reported by Santra *et al.*, their turn-over frequencies are about 300 molecules per active site per second at 300 °C for Rh(100) and Rh(110), and reach ∼330 and ∼1200 molecules per site per second on Pt(100) at 430 °C, and on Rh(100) and Rh(110) at 350 °C, respectively. The results reported by Santra *et al.* are of particular relevance to our studies because of the very similar partial pressures of the reactants applied in their and our studies. Pt_{10} clusters supported on amorphous alumina thus rank among the most active COox catalyst reported to date and can be also viewed as a model of the active site.

One feature which is seen in Fig. 1a is the apparent decrease of catalytic activity during residence at each temperature step above 150 °C, which may be associated with possible catalyst deactivation and/or poisoning. A deactivation through agglomeration can be excluded, because *in situ* GISAXS showed no evidence of sintering, as was also reported when heating Pt clusters under hydrogen.[33] A significant loss/evaporation of Pt can be excluded as well, because the fluorescence signal collected by GIXANES did not change notably during the entire temperature ramp. We hypothesize that the decay in activity
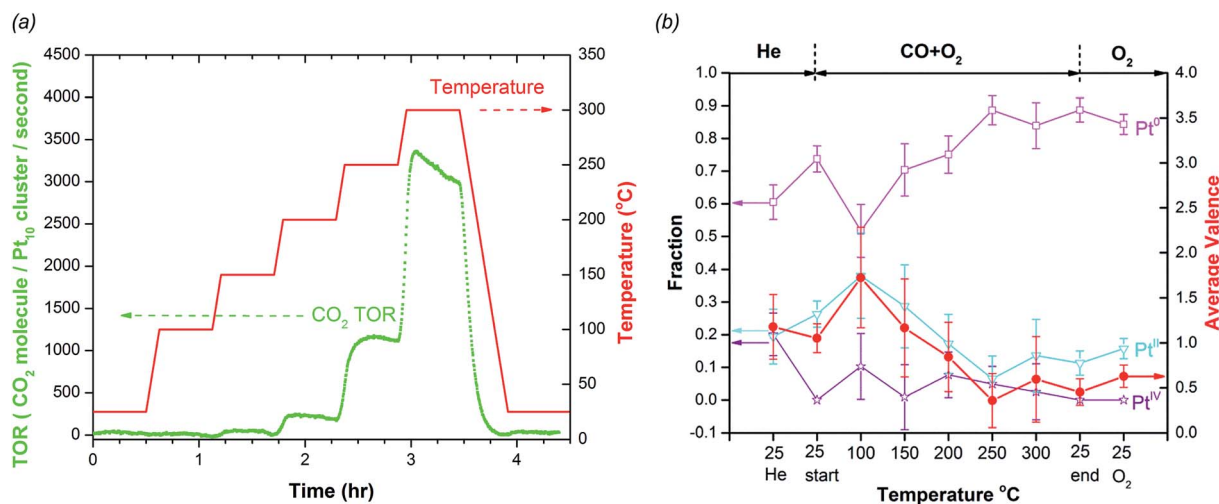
Fig. 1 (a) Temperature ramp applied (solid line) during the CO oxidation reaction, and per cluster turn-over rate as a function of temperature (dotted line). (b) Fractions of Pt components from the linear combination fitting of the *in situ* XANES spectra using Pt foil, $(NH_4)_2PtCl_4$ and PtO_2 bulk standards as the reference for Pt^0, Pt^{II} and Pt^{IV}. The calculated Pt average valence is shown with a red line and full circles.

observed here can be either caused by the initial oxygen adatoms on the cluster being gradually consumed and replaced by adsorbed CO[34,35] or due to the system undergoing structural changes (see below the discussion in the Theoretical modeling section and STM characterization). An activation energy of 60.3 ± 3.6 kJ mol^{-1} is obtained (see the Arrhenius plot in Fig. S1†), which is in very good agreement with the value of 0.6 eV (58 kJ mol^{-1}) derived from our simulations (*vide infra*) and is comparable with the lowest values reported in the literature: 65 kJ mol^{-1} for Pt_{10} clusters supported on $TiO_2(110)$ reported by Watanabe *et al.*,[11] 67 kJ mol^{-1} and 56 kJ mol^{-1} for Pt particles supported on SiO_2 reported by Herskowitz *et al.*[36] and by Cant *et al.*,[37] respectively, or 53–78 kJ mol^{-1} reported by the Somorjai group for Pt nanowires supported on various oxide supports.[31,32] The low activation energy confirms that Pt_{10} clusters on ALD-alumina are very effective COox catalysts, and the similarity of the activation energies with those reported for various Pt catalysts supported on different supports obtained under different conditions suggests that a common, robust mechanism underlies CO oxidation catalysis by Pt clusters, as will be discussed in connection with theoretical modeling below.

In situ GIXANES spectra (Fig. S2†) are collected at the Pt L_3-edge, first under helium, and then followed by exposure to the reactive gases during the temperature ramp shown in Fig. 1. At the end of the temperature ramp, the reaction cell is filled with oxygen in helium. The spectra reveal a change in white line intensity during the progress of the reaction. In order to capture the trend in the evolution of the nature of the catalyst, using spectra of powder reference materials, a linear combination fitting is performed and the results are shown in Fig. 1b. Since the Pt cluster samples are exposed to ambient conditions after the deposition in the vacuum chamber, they are initially partially oxidized as revealed by GIXANES measured under helium (labeled as 25 °C He), corresponding to an average Pt valence of ∼1.2. When the gas mixture of CO and O_2 is introduced into the reactor, some reduction is observed already at

room temperature, reflected by an average Pt valence of ∼1.0. During the temperature ramp, the clusters get more oxidized at 100 °C, with the average Pt valence increasing to ∼1.7. Above 200 °C, reduction takes place with increasing temperature, with Pt average valence stabilizing at around 0.5, indicative of a partially oxidized Pt under working conditions, as previously reported by Singh *et al.*[21] and well in tune with the oxidation state predicted by theoretical simulations reported below. After the end of the temperature ramp, the reactor was filled with 10% O_2 in He, and no obvious change in its valence state was observed during its 30 minute exposure to oxygen.

2.b STM, LEED and XPS results on Pt_{10} clusters supported on UHV-alumina

The geometry of size-selected Pt_{10} clusters soft-landed on the $Al_2O_3/NiAl(110)$ surface is investigated by STM. Fig. 2a and b show typical STM topographic images of Pt_{10} clusters deposited on $Al_2O_3/NiAl(110)$. The bright stripes are domain boundaries, appearing as line defects of the oxide film.[26,38] The topographic contrast of the domain boundaries does not arise from any height difference but from an electronic contrast effect: the geometric structure is atomically flat across the domain boundaries.[38] The observed protrusions are assigned to size-selected Pt_{10} clusters deposited on the surface. Fig. 2c shows a histogram of the apparent height distribution of the Pt_{10} clusters, from the apparent height of 0.38 ± 0.09 nm, the Pt_{10} clusters deposited on $Al_2O_3/NiAl(110)$ lay flat on the alumina surface, *i.e.* with a planar structure.[25] Note that under STM conditions of $V_s = 3.5$ V and $I_t = 0.1$ nA (V_s: sample bias, I_t: tunneling current), the apparent cluster height is overestimated by ∼0.26 nm compared with the real cluster height due to the low conductivity of the Al_2O_3 film.[27,39]

Next, we performed experiments under 800 Torr with CO and O_2 seeded in He. The concentration of CO as well as O_2 was 1% (*i.e.* partial pressures of 8 Torr) to match the reaction conditions
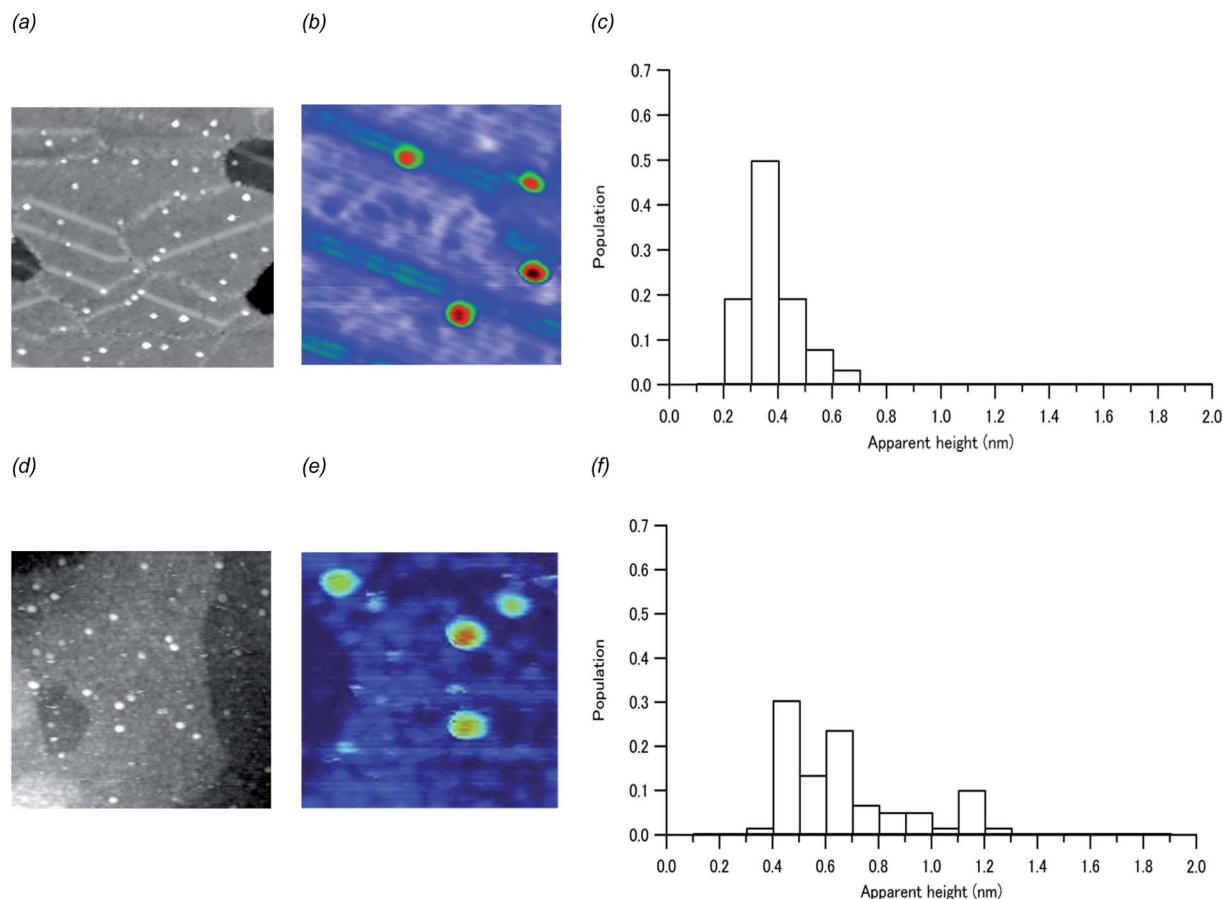
Fig. 2 (a) STM topographic image (93 × 93 nm^2, 3.5V_s, 100 pA), (b) STM topographic image (24 × 24 nm^2, 3.5V_s, 100 pA) and (c) histogram of apparent height of as-deposited clusters under vacuum at 27 °C. (d) STM topographic image (93 × 93 nm^2, 3.5V_s, 100 pA), (e) STM topographic image (24 × 24 nm^2, 3.5V_s, 100 pA), and (f) histogram of the apparent height, after CO and O$_2$ exposure at 27 °C. See Fig. S3 in the ESI† for the histograms showing the aspect ratio under vacuum as a function of temperature and Fig. S4† for the corresponding line profiles.

applied for the ALD-alumina-supported clusters. In order to distinguish between the heat-induced change and the reaction-induced change, first an annealing of the cluster sample is performed under vacuum (*i.e.* in the absence of CO and O$_2$) in the temperature range up to 200 °C, and no substantial changes in the cluster height and aspect ratio (=height/diameter) are observed (Fig. S3†). The slight decrease in the apparent height and aspect ratio at 200 °C may be consistent with the reported (partial) embedding of Pt atoms into the alumina film at >197 °C,[40] or with an incipient process of thermal morphological roughening of the substrate.

Fig. 2d and e show a typical topographic image of Pt$_{10}$/Al$_2$O$_3$/NiAl(110) after exposing the sample to the CO and O$_2$ mixture seeded in He at 27 °C under 800 Torr, while Fig. 2f depicts the histogram of the corresponding height distribution. As a crucial observation, the Pt clusters retain their density of ∼0.005 clusters per nm^2 thus excluding cluster sintering. However, the height distribution of the clusters becomes inhomogeneous, rising from ∼0.2–0.7 nm to ∼0.4–1.2 nm. We interpret this change as due to the initially two-dimensional, as-deposited Pt$_{10}$ clusters turning three-dimensional in the reactive gas environment. At variance with previous studies on similar size

Pt clusters supported on titania,[11] an exact determination of the number of Pt atomic layers is not possible on this alumina film. This is because of another striking phenomenon which is apparent in Fig. 2d, *i.e.*, the onset of a drastic change in film morphology already around room temperature, with the crystalline alumina film starting to turn amorphous, as also confirmed by LEED (Fig. S6†). The transformation of the alumina film from crystalline into amorphous accelerates at 150 °C, at which temperature the formation of bright protrusions in the film is observed as well. They cover the entire surface, making the clusters and protrusions hardly distinguishable by STM topographic observation (Fig. S5†). The morphology change in the alumina film is further illustrated by XPS (Fig. S7†), yielding an estimated thickness of the amorphous film of about 0.7 nm from the initial thickness of the crystalline alumina of 0.5 nm. The morphology change in the Al$_2$O$_3$ film would be caused by spillover of O atoms from the Pt$_{10}$ cluster to the Al$_2$O$_3$ film.[41] O$_2$ molecules in fact adsorb dissociatively on the Pt$_{10}$ cluster, followed by spillover to the Al$_2$O$_3$ film, and reaction with Al atoms at the Al$_2$O$_3$/NiAl interface. The formed Al$_2$O$_3$ is amorphous because the experimental temperature is below the crystallization temperature of Al$_2$O$_3$ (727 °C).[26]

It is intriguing to note that the final thickness of the UHV-prepared alumina after exposure to reaction conditions matches the thickness of the amorphous ALD-alumina film. Studies of the changes which the Al_2O_3/NiAl(110) phase undergoes under exposure to water[42] or oxygen[41,43] have been conducted in the literature. The findings presented here are entirely consistent with these previous studies, such as *e.g.* the transition from crystalline to amorphous morphology[42] and the thickening of the film from 0.5 to ≈ 0.7 nm, especially facile in the presence of deposited metal clusters.[41,43]

2.c Theoretical modeling – gas phase and supported Pt_{10} clusters and their COox activity

Starting from gas phase Pt_{10} species, a few low-energy isomers of bare Pt_{10} are reported in Fig. 3a and S8a and d† as derived from a global optimization search. The Pt_{10} putative global minimum has a pyramidal shape, and the overall structural landscape is consistent with previous reports[44] showing this is the size at which the 2D → 3D structural transition is complete. The adsorption of O_2 or CO intact molecules on these clusters is energetically favorable by 0.7–0.8 eV and 1.6–2.1 eV, respectively, which preferentially occurs on low-coordinated Pt atoms, while O_2 dissociation lowers the energy by 1.12–2.34 eV (Fig. 3b and S8b and c). For Pt_{10} deposited on an alumina surface (Fig. 4a and S9a†), a bilayer structure becomes the lowest-energy supported configuration. Adsorption of O_2 and CO intact molecules onto the pyramidal and bilayer structures of Pt_{10}@Al_2O_3 (Fig. 4b and c and S9b and c†) corresponds to an adsorption energy of 1.93–2.13 eV for CO, and 0.81–1.60 eV for oxygen, respectively. The strong increase of O_2 adsorption energy up to ~1.6 eV in the supported case is consistent with oxygen activation at the metal/oxide interface,[9,22,23,45] and plays a role in promoting O_2 and CO co-adsorption which is beneficial to catalytic activity.[46,47]

Two mechanisms are operative for the CO oxidation catalytic reaction: (i) O_2 breaking followed by the reaction of O adatoms with CO, and (ii) interaction of adsorbed O_2 with CO (pre-adsorbed on the metal cluster in a Langmuir–Hinshelwood mechanism or coming from the gas phase in an Eley–Rideal one) to produce an OOCO adsorbed intermediate which then produces adsorbed O plus CO_2 or evolves into a carbonate (CO_3) adduct.[47,48] O_2 breaking is thermodynamically favored (Fig. 3b and 4b) and can occur with a low (≈ 0.3 eV) energy barrier but only starting from O_2 adsorbed on a bridge site of Pt_{10} (Fig. S10† and the last two images of Fig. 4b). Bridge adsorption is however disfavored at high CO coverage henceforth increasing in the barrier to O_2 breaking to nearly 2 eV from our simulations. The OOCO mechanism then becomes competitive: CO and O_2 co-adsorb on free Pt_{10} and evolve CO_2 and O with a barrier of only 0.6 eV (Fig. 3c). This conclusion is in tune with previous studies[49] showing that the mechanism of CO oxidation changes from O_2 direct dissociation at low CO coverage to an OOCO mechanism at high CO coverage. Note that[47] the formation of the thermodynamically most favored CO_3 carbonate species (Fig. 3c) has a non-negligible energy barrier, which kinetically favors CO_2 desorption, as confirmed by a Car–Parrinello Molecular Dynamics simulation (Fig. S11†). The barrier of the OOCO mechanism in the supported case Fig. 4d is also ≈ 0.6 eV. Adsorbed O on the resulting $Pt_{10}O(CO)_n$ cluster then easily reacts with an incoming CO to produce CO_2. The agreement of these simulations with the experiment is very good. The predicted barrier of ≈ 0.6 eV (57.8 kJ mol^{-1}) is within the experimental range of the effective energy barrier (60.3 ± 3.6 kJ mol^{-1}). The experimental evidence of an initially high Pt oxidation state which progressively reduces as the COox reaction proceeds is rationalized as due to an initial $Pt_{10}O_x$ oxidized cluster[46,50] under ambient conditions which transforms into the catalytically active species after the introduction of CO. The observed catalyst deactivation at high temperature is also explained as due to the formation of inactive CO_3 species (Fig. 3c) whose formation presents a kinetic barrier, which becomes less important as the temperature increases. This hypothesis is supported by experiment: carbon-1s XPS spectra (Fig. S7b†) show that a broad peak at 290.5 eV evolves only at high temperature, which is associated with the formation of highly oxidized species such as a carbonate group (an
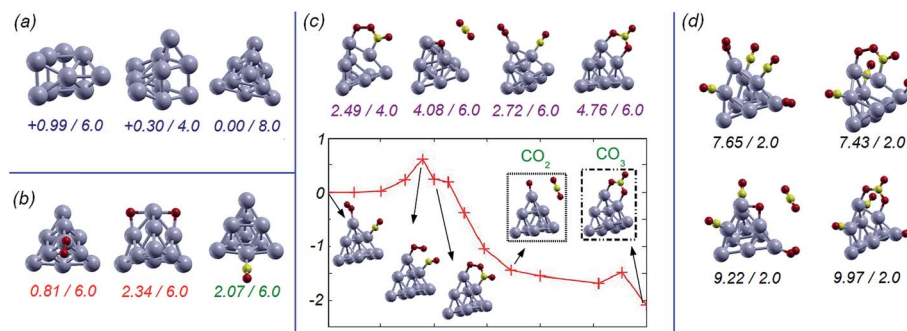

Fig. 3 (a) Structures with relative energies/total spin of three distinct lowest-energy minima of gas-phase Pt_{10}. In (b) adsorption energy/total spin of O_2, O + O and CO species on the global minimum of gas-phase Pt_{10} are shown for the most stable sites found in each case (values in red for O_2 and O + O, green for CO, respectively). (c) Top row: energy of adsorption/total spin corresponding to co-adsorption of CO/O_2 species on the global minimum of gas-phase Pt_{10}; bottom, a path leading to CO_2 and CO_3 formation: each red cross represents one NEB image of a climbing-image NEB procedure. (d) Adsorption energy/total spin for the locally saturated $Pt_{10}(O_2)_2(CO)_3$ cluster in successive configurations leading to the formation of gas-phase CO_2 or adsorbed CO_3. Energies in eV and total spin in bohr.
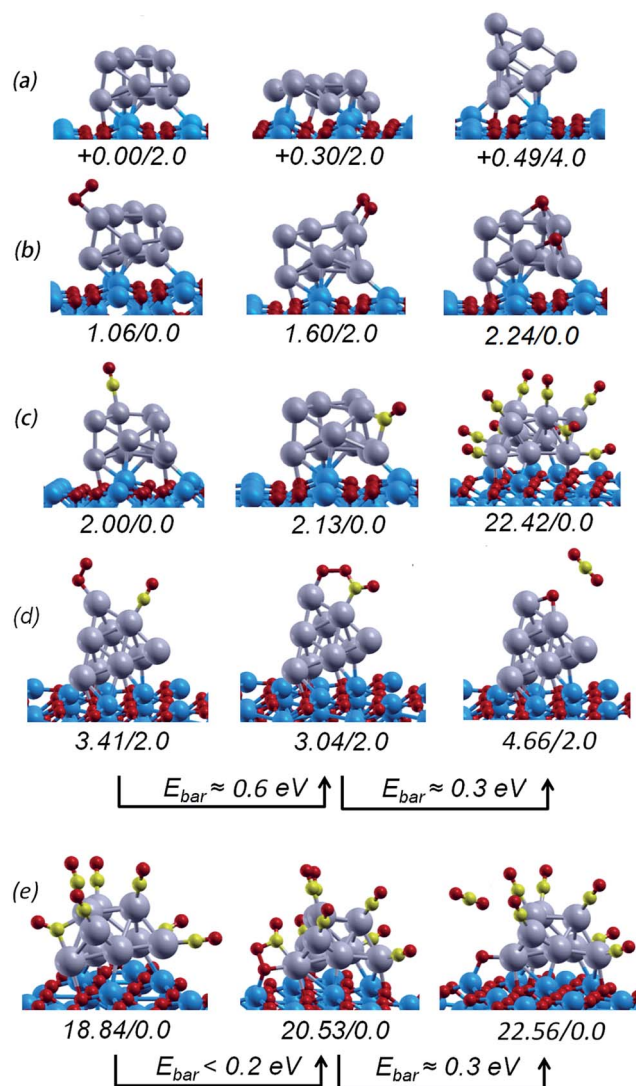
This journal is © The Royal Society of Chemistry 2017

J. Mater. Chem. A, 2017, **5**, 4923–4931 | **4927**

(a) +0.00/2.0   +0.30/2.0   +0.49/4.0

(b) 1.06/0.0   1.60/2.0   2.24/0.0

(c) 2.00/0.0   2.13/0.0   22.42/0.0

(d) 3.41/2.0   3.04/2.0   4.66/2.0

$E_{bar} \approx 0.6$ eV ↑ $E_{bar} \approx 0.3$ eV ↑

(e) 18.84/0.0   20.53/0.0   22.56/0.0

$E_{bar} < 0.2$ eV ↑ $E_{bar} \approx 0.3$ eV ↑

Fig. 4 (a) Relative energies/total spin of the most stable structures of Pt_{10}/Al_2O_3. (b–d) Adsorption energies/total spin of: (b) O_2, (c) CO and (d and e) CO + O_2 species on Pt_{10}/Al_2O_3. In (d and e) the energy barriers of selected adsorption and reaction processes are also reported as E_{bar}. Energy values in eV and spin in bohr. See the text for details.

additional peak at 285.6 eV also appears which could be due to more complex C–C–O species).

To investigate ligand coverage effects, we locally saturate the bare Pt_{10} cluster around one tip with one O_2 and several CO (Fig. 3d and S12†) and investigate the OOCO mechanism. The energetics of adsorption steps on the saturated cluster closely parallels that at low coverage (Fig. 3c). Taking as zero the energy of the co-adsorbed CO + O_2 species, we find in fact the following relative energies: OOCO = 0.23 *vs.* 0.22 eV, O + CO_2 = −1.36 *vs.* −1.57 eV, and CO_3 = −2.04 *vs.* −2.32 eV, for low and high coverage, respectively, and also the energy barriers are very similar to the low-coverage *régime*. Moreover, for supported clusters, due to the support-enhanced oxygen adsorption,[45] a further mechanism is operative (Fig. 4e): the fully CO-saturated supported global minimum of Pt_{10}, thanks to the

stabilizing electric field[22,45,47,48] from the alumina substrate, can co-adsorb O_2 at the interface with the substrate, produce an OOCO intermediate, and successively evolve free CO_2 and an O adatom with an overall energy barrier of ≈0.3 eV (Fig. 4e and S9f†). In contrast to larger particles in which well-coordinated Pt sites are apparently the active sites CO oxidation,[51] here we thus find that the cluster/support interface plays a crucial role at high CO coverage: O_2 can in fact adsorb at these sites strongly enough to avoid CO poisoning issues and catalyze COox *via* an OOCO intermediate.[22,45,47] The present findings can be compared with the different phenomenology encountered in COox nanocatalysts made up of other metal elements or by Pt nanoparticles but with larger sizes. For example, the catalytic activity of Ir nanoparticles in COox seems to be rather structure-independent,[52] whereas in Pt this effect is thought to be significant although masked in larger nanoparticles by reshaping and restructuring under reaction conditions.[51] COox on gold (sub-)nanoaggregates has also been widely investigated.[53] In particular, Au sub-nanometer clusters have been proved to be highly active catalysts, especially when in the form of two-atomic-layer-thick systems,[54] and a strong effect of cluster/support interface has been claimed to be important[45] as here in the Pt_{10} catalyst at high coverage, with a possible role of charge transfer.[55]

Finally, for completeness in Fig. S13† we report a Bader charge analysis of two selected configurations: $Pt_{10}(O_2)_2(CO)_3$ and $Pt_{10}O_2(CO)_2(O)_2$, *i.e.*, contrasting un-dissociated and dissociated O_2. A charge transfer from Pt_{10} to O_2 (and to a lesser extent CO) which further increases when the oxygen molecule dissociates is clearly apparent from this figure, thus rationalizing the experimentally observed mildly oxidized state of Pt under reaction conditions.

3. Conclusions

In summary, the results of an in-depth investigation of CO oxidation by alumina-supported Pt_{10} clusters are presented by combining experiments using size-selected clusters under UHV and atmospheric pressure conditions and theoretical modeling into a single interdisciplinary approach, yielding fundamental insights about the structural properties and catalytic activity of Pt_{10} clusters in CO oxidation. The Pt_{10}/ALD-alumina is not only a realistic model of the active site in real-world catalytic materials but also turns out to be sintering resistant under catalytic conditions and highly active with a TOR of 335 molecules per second per Pt atom at 300 °C (among the most active reported CO oxidation catalysts). Notably, under reaction conditions the initially crystalline UHV-alumina film transforms akin to the amorphous ALD-alumina film, accompanied by Pt_{10} clusters transforming from planar into a three-dimensional structure and exhibiting a similar COox catalytic activity. DFT simulations reveal the details of the potential energy landscape of bare and CO/O_2-covered Pt_{10} clusters, predicting a 3D structure for Pt_{10}, an energy barrier of ≈58 kJ mol^{-1} for CO oxidation and an intermediate Pt oxidation state, in excellent agreement with experimental findings. The present study contributes to bridge the material (support) gap in heterogeneous nanocatalysis by

4928 | *J. Mater. Chem. A*, 2017, **5**, 4923–4931

This journal is © The Royal Society of Chemistry 2017

interconnecting surface-science and real-world experiments, and to further single out sub-nanometer (or ultra-nano) metal clusters as unique catalytic systems,[10] all this supported by first-principles theoretical analysis.

4. Methods

The ALD-alumina supported Pt_{10} catalyst used in the *in situ* studies was fabricated by soft-landing size-selected metal clusters from a molecular beam generated in a laser vaporization source.[23,24] Here we deposited positively charged clusters consisting of dominantly 10-atom clusters, with traces (about ~10%) of 8 and 9-atom clusters, on the alumina support kept at room temperature.

The catalyst was characterized in an *in situ* GISAXS/GIXANES/TPRx continuous fixed-bed flow reactor of own design[56] using a gas mixture of 1% CO and 1% O_2 seeded in He at a total pressure of 800 Torr. The applied temperature profile is depicted in Fig. 1a. The turn-over rate (TOR) data reported were background corrected by subtracting the mass spectrometer CO_2 signal measured for a ALD-blank alumina support (*i.e.* sample without clusters) from the signal measured on the Pt_{10}/ALD-alumina; then the CO_2 signal is converted into TOR based on the known Pt metal loading, on Pt atoms or Pt_{10} cluster basis. GIXANES was detected in fluorescence mode at Pt L_3 edge to determine the evolution of the oxidation state of Pt during the reaction. GISAXS with a geometry optimized for particles above 1 nm was used to monitor possible sintering during the course of the reaction.

The size-selected Pt_{10} cluster ions used in the UHV/surface characterization studies were produced by a dc magnetron sputtering[57] and deposited under soft-landing conditions on the crystalline alumina film grown on the top of a NiAl(110) crystal (Al_2O_3/NiAl(110)).[58] The impact energy is tuned to 0.67 eV per atom by adjusting a bias voltage applied to the surface (soft-landing condition). STM measurements are performed at room temperature with a tungsten tip. We performed the high-pressure gas treatment using the high-pressure reaction cell[57] under identical conditions as applied in the *in situ* experiments at Argonne for the Pt_{10}/ALD-alumina system, under 800 Torr. LEED measurements were performed with an electron kinetic energy of 50 eV at room temperature. XPS measurements were carried out using non-monochromatized Mg Kα (1253.6 eV) radiation from a dual-anode X-ray source, along with a hemispherical energy analyzer. XPS spectra were taken at an electron take-off angle of 40 degree with a pass energy of 20 eV at room temperature.

DFT calculations employed the Perdew–Burke–Ernzerhof (PBE)[59] exchange–correlation functional and two different periodic codes for free and supported clusters, respectively: the Quantum Espresso[60] plane-wave self-consistent field code (PWscf), employing ultra-soft pseudopotentials,[61] and the Vienna *ab initio* Simulation Package (VASP),[62] with the electron–ion interaction described by the full-potential all-electron projector augmented wave (PAW) method.[63] The α-Al_2O_3(0001) surface was modeled with a 18-atomic layer slab by truncating the bulk α-Al_2O_3 structure, separated by a vacuum of 13 Å

between periodic slabs. It should be noted that an atomistic structural model of the ultrathin alumina phase obtained under ultra-high vacuum (UHV) conditions by oxidation of the NiAl(110) surface exists.[64] However we have not used this model in our simulations and used the α-Al_2O_3(0001) surface as a model instead for two main reasons: (i) the unit cell of the ultrathin alumina[64] is too large to be affordable by our computational resources, especially considering that a systematic sampling of a deposited Pt_{10} cluster with additional CO and O_2 molecules or O atoms adsorbed should have been considered as we have successfully realized on smaller unit cells; (ii) experiments in the present and previous[41–43] work indicate that the crystalline ultrathin alumina support transforms under reaction conditions into an amorphous phase, whose structure is unknown – we therefore used the Pt_{10} cluster in the gas-phase and deposited onto the α-Al_2O_3(0001) surface to bracket the support effect between zero and a strongly interacting surface. However, considering that the surface of the structural model unveiled in ref. 64 presents a unique and very interesting pattern of 5-fold and 7-fold sites, it would be very interesting to investigate its use as a catalytic support – this is left for future work. After a preliminary scan using lower-accuracy parameters, geometry optimizations were performed spin unrestricted and using high accuracy: wave-function/charge-density cutoffs of 40/320 Ry, respectively, and 5 × 5 × 1 set of *k*-points for integration in reciprocal space. The search for the most stable structures for the Pt_{10} cluster in the gas phase was performed using a Basin-Hopping (BH) global search algorithm[65,66] coupled with a DFT evaluation of energy and forces. Structural search for supported clusters was less exhaustive due to the cpu-demanding character of such simulations. Configurations selected from the most stable structures in the gas phase according to previous experience were positioned on the alumina surface, trying to explore as diverse an epitaxy as possible, and locally minimized. Transition states were determined using the nudged elastic band (NEB) algorithm using the Broyden scheme using 5–8 intermediate images.

Further details about the methods are provided in the ESI.†

This journal is © The Royal Society of Chemistry 2017

J. Mater. Chem. A, 2017, **5**, 4923–4931 | **4929**

References

1 G. Ertl, *Surf. Sci.*, 1993, **287–288**, 1–11.

2 J. T. Kummer, *Energy Combust. Sci.*, 1980, **6**, 177–199.

3 R. Farrauto, S. Hwang, L. Shore, W. Ruettinger, J. Lampert, T. Giroux, Y. Liu and O. Ilinich, *Annu. Rev. Mater. Res.*, 2003, **33**, 1–27.

4 G. A. Somorjai and G. Rupprechter, *J. Phys. Chem. B*, 1999, **103**, 1623–1638.

5 J. Libuda and H.-J. Freund, *Surf. Sci. Rep.*, 2005, **57**, 157–298.

6 B. Qiao, A. Wang, X. Yang, L. F. Allard, Z. Jiang, Y. Cui, J. Liu, J. Li and T. Zhang, *Nat. Chem.*, 2011, **3**, 634–641.

7 J. D. Kistler, N. Chotigkrai, P. Xu, B. Enderle, P. Praserthdam, C. Y. Chen, N. D. Browning and B. C. Gates, *Angew. Chem.*, 2014, **53**, 8904–8907.

8 K. Ding, A. Gulec, A. M. Johnson, N. M. Schweitzer, G. D. Stucky, L. D. Marks and P. C. Stair, *Science*, 2015, **350**, 189–192.

9 U. Heiz, A. Sanchez, S. Abbet and W. D. Schneider, *J. Am. Chem. Soc.*, 1999, **121**, 3214–3217.

10 E. C. Tyo and S. Vajda, *Nat. Nanotechnol.*, 2015, **10**, 577–588.

11 Y. Watanabe, X. Wu, H. Hirata and N. Isomura, *Catal. Sci. Technol.*, 2011, **1**, 1490–1495.

12 W. E. Kaden, T. Wu, W. A. Kunkel and S. L. Anderson, *Science*, 2009, **326**, 826–829.

13 S. Lee, C. Fan, T. Wu and S. L. Anderson, *J. Am. Chem. Soc.*, 2004, **126**, 5683–5684.

14 T. Imaoka, H. Kitazawa, W. J. Chun, S. Omura, K. Albrecht and K. Yamamoto, *J. Am. Chem. Soc.*, 2013, **135**, 13089–13095.

15 G. Kwon, G. A. Ferguson, C. J. Heard, E. C. Tyo, C. Yin, J. DeBartolo, S. Seifert, R. E. Winans, A. J. Kropf, J. Greeley, R. L. Johnston, L. A. Curtiss, M. J. Pellin and S. Vajda, *ACS Nano*, 2013, **7**, 5808–5817.

16 S. Bonanni, K. Aït-Mansour, W. Harbich and H. Brune, *J. Am. Chem. Soc.*, 2012, **134**, 3445–3450.

17 S. Lee, M. Di Vece, B. Lee, S. Seifert, R. E. Winans and S. Vajda, *ChemCatChem*, 2012, **4**, 1632–1637.

18 S. Lee, B. Lee, S. Seifert, R. E. Winans and S. Vajda, *J. Phys. Chem. C*, 2015, **119**, 11210–11216.

19 G. A. Ferguson, C. Yin, G. Kwon, E. C. Tyo, S. Lee, J. P. Greeley, P. Zapol, B. Lee, S. Seifert, R. E. Winans, S. Vajda and L. A. Curtiss, *J. Phys. Chem. C*, 2012, **116**, 24027–24034.

20 J. A. Anderson, *J. Chem. Soc., Faraday Trans.*, 1992, **88**, 1197–1201.

21 J. Singh, E. M. C. Alayon, M. Tromp, O. V. Safonova, P. Glatzel, M. Nachtegaal, R. Frahm and J. A. van Bokhoven, *Angew. Chem.*, 2008, **47**, 9260–9264.

22 F. R. Negreiros, E. Apra, G. Barcaro, L. Sementa, S. Vajda and A. Fortunelli, *Nanoscale*, 2012, **4**, 1208–1219.

23 Y. Lei, F. Mehmood, S. Lee, J. Greeley, B. Lee, S. Seifert, R. E. Winans, J. W. Elam, R. J. Meyer, P. C. Redfern, D. Teschner, R. Schlögl, M. J. Pellin, L. A. Curtiss and S. Vajda, *Science*, 2010, **328**, 224–228.

24 S. Vajda, M. J. Pellin, J. P. Greeley, C. L. Marshall, L. A. Curtiss, G. A. Ballentine, J. W. Elam, S. Catillon-Mucherie, P. C. Redfern, F. Mehmood and P. Zapol, *Nat. Mater.*, 2009, **8**, 213–216.

25 V. Habibpour, M. Y. Song, Z. W. Wang, J. Cookson, C. M. Brown, P. T. Bishop and R. E. Palmer, *J. Phys. Chem. C*, 2012, **116**, 26295–26299.

26 R. M. Jaeger, H. Kuhlenbeck, H. J. Freund, M. Wuttig, W. Hoffmann, R. Franchy and H. Ibach, *Surf. Sci.*, 1991, **259**, 235–252.

27 A. Beniya, N. Isomura, H. Hirata and Y. Watanabe, *Phys. Chem. Chem. Phys.*, 2014, **16**, 26485–26492.

28 H. Yasumatsu and N. Fukui, *Phys. Chem. Chem. Phys.*, 2014, **16**, 26493–26499.

29 J. M. Thomas, *J. Chem. Phys.*, 2008, **128**, 182502.

30 A. K. Santra and D. W. Goodman, *Electrochim. Acta*, 2002, **47**, 3595–3609.

31 X. M. Yan, S. Kwon, A. M. Contreras, M. M. Koebel, J. Bokor and G. A. Somorjai, *Catal. Lett.*, 2005, **105**, 127–132.

32 A. M. Contreras, X. M. Yan, S. Kwon, J. Bokor and G. A. Somorjai, *Catal. Lett.*, 2006, **111**, 5–13.

33 R. E. Winans, S. Vajda, G. E. Ballentine, J. W. Elam, B. Lee, M. J. Pellin, S. Seifert, G. Y. Tikhonov and N. A. Tomczyk, *Top. Catal.*, 2006, **39**, 145–149.

34 N. W. Cant and D. E. Angove, *J. Catal.*, 1986, **97**, 36–42.

35 I. Nakai, H. Kondoh, K. Amemiya, M. Nagasaka, T. Shimada, R. Yokota, A. Nambu and T. Ohta, *J. Chem. Phys.*, 2005, **122**, 134709.

36 M. Herskowitz, R. Holliday, M. B. Cutlip and C. N. Kenney, *J. Catal.*, 1982, **74**, 408–410.

37 N. W. Cant, P. C. Hicks and B. S. Lennon, *J. Catal.*, 1978, **54**, 372–383.

38 G. H. Simon, T. Konig, L. Heinke, L. Lichtenstein, M. Heyde and H. J. Freund, *New J. Phys.*, 2011, **13**, 123028.

39 K. H. Hansen, T. Worren, E. Lægsgaard, F. Besenbacher and I. Stensgaard, *Surf. Sci.*, 2001, **475**, 96.

40 T. Bertrams, F. Winkelmann, T. Uttich, H.-J. Freund and H. Neddermayer, *Surf. Sci.*, 1995, **331**, 1515–1519.

41 S. Shaikhutdinov, M. Heemeier, J. Hoffmann, I. Meusel, B. Richter, M. Bäumer, H. Kuhlenbeck, J. Libuda, H. J. Freund, R. Oldman, S. D. Jackson, C. Konvicka, M. Schmid and P. Varga, *Surf. Sci.*, 2002, **501**, 270–281.

42 V. Maurice, N. Frémy and P. Marcus, *Surf. Sci.*, 2005, **581**, 88–104.

43 L. Gragnaniello, T. Ma, G. Barcaro, L. Sementa, F. R. Negreiros, A. Fortunelli, S. Surnev and F. P. Netzer, *Phys. Rev. Lett.*, 2012, **108**, 195507.

44 K. Bhattacharyya and C. Majumder, *Chem. Phys. Lett.*, 2007, **446**, 374–379.

45 L. Molina, M. D. Rasmussen and B. Hammer, *J. Chem. Phys.*, 2004, **120**, 7673–7680.

46 F. Gao, S. M. McClure, Y. Cai, K. K. Gath, Y. Wang, M. S. Chen, Q. L. Guo and D. W. Goodman, *Surf. Sci.*, 2009, **603**, 65–70.

47 F. R. Negreiros, L. Sementa, G. Barcaro, S. Vajda, E. Aprá and A. Fortunelli, *ACS Catal.*, 2012, **2**, 1860–1864.

48 A. D. Allian, K. Takanabe, K. L. Fujdala, X. Hao, T. J. Truex, J. Cai, C. Buda, M. Neurock and E. Iglesia, *J. Am. Chem. Soc.*, 2011, **133**(12), 4498–4517.

49 H. Zhou, X. Cheng and J. Wang, *Int. J. Quantum Chem.*, 2016, **116**, 939–944.

50 S. Kunz, F. F. Schweinberger, V. Habibpour, M. Röttgen, C. Harding, M. Arenz and U. Heiz, *J. Phys. Chem. C*, 2009, **114**, 1651–1654.

51 M. J. Kale and P. Cristopher, *ACS Catal.*, 2016, **6**, 5599–5609.

52 M. Sushchikh, L. Cameron, H. Metiu and E. W. McFarland, *Int. J. Chem. Kinet.*, 2008, **40**, 826–830.

53 G. C. Bond and D. T. Thompson, *Catal. Rev.: Sci. Eng.*, 1999, **41**, 319–388.

54 A. A. Herzing, C. J. Kiely, A. F. Carley, P. Landon and G. J. Hutchings, *Science*, 2008, **321**, 1331–1335.

55 B. Yoon, H. Hakkinen, U. Landman, A. S. Worz, J. M. Antonietti, S. Abbet, K. Judai and U. Heiz, *Science*, 2005, **307**, 403–407.

56 S. Lee, B. Lee, S. Seifert, S. Vajda and R. E. Winans, *Nucl. Instrum. Methods Phys. Res., Sect. A*, 2011, **649**, 200–203.

57 Y. Watanabe and N. Isomura, *J. Vac. Sci. Technol., A*, 2009, **27**, 1153–1158.

58 A. Piednoir, E. Perrot, S. Granjeaud, A. Humbert, C. Chapon and C. R. Henry, *Surf. Sci.*, 1997, **391**, 19–26.

59 J. P. Perdew, K. Burke and M. Ernzerhof, *Phys. Rev. Lett.*, 1996, **77**, 3865–3868.

60 P. Giannozzi, S. Baroni, N. Bonini, M. Calandra, R. Car, C. Cavazzoni, D. Ceresoli, G. Chiarotti, M. Cococcioni, I. Dabo, *et al.*, *J. Phys.: Condens. Matter*, 2009, **21**, 395502.

61 D. Vanderbilt, *Phys. Rev. B: Condens. Matter Mater. Phys.*, 1990, **41**, 7892–7895.

62 G. Kresse and J. Furthmüller, *Phys. Rev. B: Condens. Matter Mater. Phys.*, 1996, **54**, 11169–11186.

63 P. E. Blöchl, *Phys. Rev. B: Condens. Matter Mater. Phys.*, 1994, **50**, 17953–17979.

64 G. Kresse, M. Schmid, E. Napetschnig, M. Shishkin, L. Köhler and P. Varga, *Science*, 2005, **308**, 1440–1442.

65 E. Aprà, R. Ferrando and A. Fortunelli, *Phys. Rev. B: Condens. Matter Mater. Phys.*, 2006, **73**, 205414.

66 G. Barcaro, E. Aprà and A. Fortunelli, *Chem.–Eur. J.*, 2007, **13**, 6408–6418.

This journal is © The Royal Society of Chemistry 2017

J. Mater. Chem. A, 2017, **5**, 4923–4931 | **4931**